Confinement-driven emergence of hyperuniform fluids

Fabio Leoni [1,*] Giancarlo Franzese [2,3,†] Erdal C. Oğuz [4,5,6,‡] and Fausto Martelli [1,7,§]

[1]Dipartimento di Fisica, Università degli Studi di Roma La Sapienza, Piazzale Aldo Moro 5, Rome 00185, Italy
[2]Secció de Física Estadística i Interdisciplinària, Departament de Física de la Matèria Condensada, Universitat de Barcelona, Martí i Franquès 1, 08028 Barcelona, Spain
[3]Institut de Nanociència i Nanotecnologia, Universitat de Barcelona, Barcelona, Spain
[4]Key Laboratory of Soft Matter Physics, Institute of Physics, Chinese Academy of Sciences, Beijing 100190, China
[5]Songshan Lake Materials Laboratory, Dongguan, Guangdong 523808, China
[6]School of Chemistry and the Center for Physics and Chemistry of Living Systems, Tel Aviv University, Tel Aviv 6997801, Israel
[7]CNR-Istituto dei Sistemi Complessi, Piazzale Aldo Moro 5, Rome 00185, Italy

(Received 9 June 2025; revised 13 October 2025; accepted 26 November 2025; published 16 December 2025)

Controlling emergent structural order in spatially constrained systems is a fundamental challenge. Using large-scale simulations of a model fluid at equilibrium conditions, we show that geometric confinement alone can stabilize fluid and hyperuniform labyrinthine phases. Moreover, confinement can induce self-assembly into distinct regimes—ranging from nonhyperuniform to antihyperuniform configurations—providing a robust mechanism for tuning spatial order. Our results identify confinement as a minimal design principle for engineering systems with target structural properties, including (anti)hyperuniformity, without relying on genetic or chemical specificity, and with broad applications in multiple disciplines and technologies.

DOI: 10.1103/9xrg-4684

I. INTRODUCTION

Confined fluids are ubiquitous in numerous scientific and technological contexts, including biology, nanotechnology, and microfluidics. The thermodynamic, dynamic, and structural characteristics of these fluids can be profoundly modified by the degree of confinement and the specific geometry of the confining environment [1–11]. At the nanoscale, boundary interactions shape phase behavior: Attractive walls enhance ordering and freezing, while repulsive boundaries suppress crystallization by amplifying density fluctuations [12–14]—though exceptions, such as mono/bilayer water ice formation in graphene slit pores, exist [15,16].

Beyond modifying bulk properties, confinement directs self-assembly, stabilizing emergent phases that depend on the confining geometry. Cylindrical or spherical confinement yields helices and concentric layers [17–20], while slit pores favor layered arrangements including structured yet fluid-like states [21–25], as seen in confined water and complex liquids [3,6,26,27]. The nature of the confining boundaries—soft, as in biological systems, or hard, as in (multi)graphene enclosures—can impose long-range structural perturbations [26,28,29]. Despite extensive research into the effects of confinement on fluid properties, the mechanisms by which confinement governs structural order remain insufficiently understood. This open question has far-reaching implications across disciplines and technologies. It forms the central focus of the present study, with particular emphasis on emergent hyperuniform (or superhomogeneous [30]) and long-range structural organization. Disordered hyperuniformity is a striking form of long-range order in which density fluctuations are anomalously suppressed at large scales, akin to crystalline solids, yet without periodic or quasiperiodic order. Hyperuniform states are characterized by a vanishing structure factor at small wavenumbers, $\lim_{|\mathbf{k}|\to 0} S(\mathbf{k}) = 0$ [31]. The ratio $H = S(0)/S(k')$, where k' is the wavenumber at the largest peak height of $S(k)$, measures how close a system is to perfect hyperuniformity [32]. Systems in which $H \lesssim 10^{-3}$ are deemed to be nearly hyperuniform. Such degree of hyperuniformity has been detected in out-of-equilibrium systems as different as jammed packings, amorphous materials, active matter, open quantum systems, biological tissues, ecosystems, and neural networks [33–50], among others. On the other hand, achieving disordered hyperuniformity in equilibrium fluids remains challenging.

Here, we conduct large-scale molecular dynamics simulations of a complex fluid at equilibrium conditions confined within slit pores across a range of densities and temperatures. Within a specific density regime, the fluid spontaneously self-organizes into two-dimensional (2D) layers with hyperuniform, labyrinthine structures ($H \lesssim 10^{-3}$)—an emergent behavior that persists across different system sizes and confinement geometries. Additionally, we identify a broad class

*Contact author: fabio.leoni@uniroma1.it
†Contact author: gfranzese@ub.edu
‡Contact author: ecoguz@iphy.ac.cn
§Contact author: fausto.martelli@cnr.it

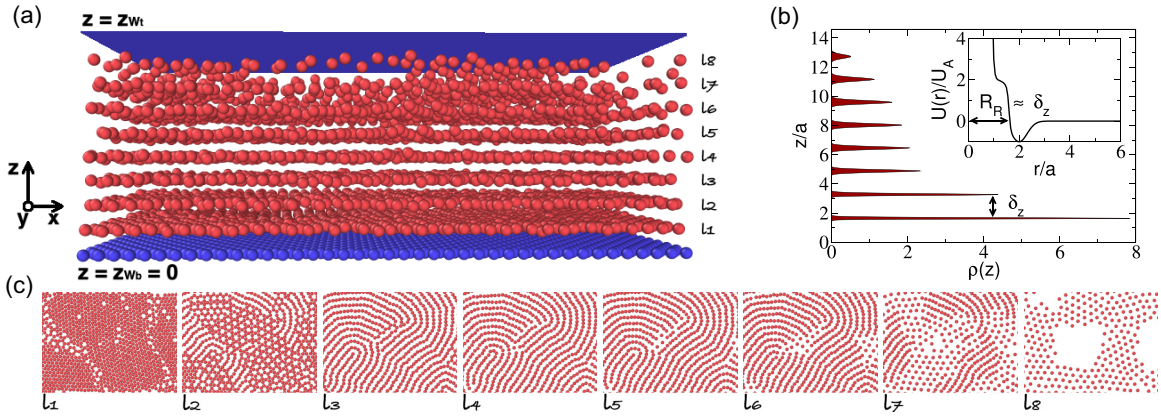

FIG. 1. The CSW fluid under slit-pore confinement. (a) Representative simulation snapshot showing a small section of the confined fluid (red particles) at $\rho = 0.3$ and $T = 0.3$ after rapid annealing and equilibration ($\tau = t_0$). The confinement between two parallel walls (blue: bottom wall attractive, top wall repulsive) produces eight well-defined layers, labeled $l_1, l_2, \ldots, l_8$ from the attractive wall outward. (b) The density profile along the z axis characterizes the layers, with the interlayer spacing δ_z approximately matching the repulsive radius R_R of the CSW potential [inset in panel (b)]. (c) Snapshots of a subregion (50×30 in units of a) in the xy plane ($\simeq 2.6\%$ of the total system area) for each layer labeled as l_i (where $i = 1, \ldots, 8$), highlighting the particle arrangement within individual layers.

of effectively antihyperuniform layers ($H \gtrsim 10^1$), characterized by long-wavelength density fluctuations that exceed those of a Poissonian reference (frequently arising near criticality or in regimes prone to cavitation [51]).

Our findings demonstrate that confinement-based protocols provide a tunable, robust, and theoretically grounded strategy for engineering hyperuniform and antihyperuniform fluids under equilibrium conditions. By exploiting confinement as a design parameter, this approach enables precise control over long-range structural correlations, offering practical pathways for the development of advanced materials and nanofluidic systems.

II. MODEL

We perform large-scale molecular dynamics simulations of an anomalous liquid as a prototypical example of a complex fluid, modeled by a continuous sholdered well (CSW) potential [2], confined in a slit pore with an attractive structured bottom wall and a repulsive structureless top wall [Fig. 1(a)]. The CSW fluid belongs to the category of isotropic soft-core models with two characteristic length scales, which coarse-grain the interactions of solids featuring different crystal phases (polymorphs) or amorphous states (polyamorphs), as well as fluids exhibiting unusual properties, such as structural, diffusion, and density anomalies. They have been shown to describe properties of complex liquids, including colloidal suspensions, protein solutions, or liquid metals and, to a limited extent, water [52]. The CSW effective interaction potential between two particles at a distance r is [Fig. 1(b)]

$$U(r) \equiv \frac{U_R}{1 + \exp(\Delta(r - R_R)/a)} - U_A \exp\left[-\frac{(r - R_A)^2}{2\delta_A^2}\right] + U_A\left(\frac{a}{r}\right)^{24}, \qquad (1)$$

where R_A and R_R represent the distances of the attractive minimum and the repulsive radius, respectively; U_A and U_R are the energies of the attractive well and the repulsive shoulder, respectively; δ_A^2 is the variance of the Gaussian centered at R_A; and Δ is the parameter controlling the slope between the shoulder and the well at R_R.

We set the parameters $U_R/U_A = 2$, $R_R/a = 1.6$, $R_A/a = 2.0$, and $(\delta_A/a)^2 = 0.1$, following Refs. [2,53,54]. We also use $\Delta = 30$, consistent with previous bulk studies [53]. We use LAMMPS [55] to simulate the system in the NVT ensemble, where N is the number of particles, V the volume of the simulation box, and T the temperature. Temperature, density, length, and time are expressed in reduced units: $T^* \equiv k_B T/U_A$, $\rho^* \equiv \rho a^3$, $r^* \equiv r/a$, and $t^* \equiv (a^2 m/U_A)^{1/2}$. For clarity, reduced units are used throughout the manuscript without the asterisk notation. Further details on the model, simulation parameters, wall structures, and annealing protocols can be found in the Supplemental Material [56].

III. RESULTS

In our investigation, we systematically vary density and temperature, performing thermal annealing at two different rates to explore emergent structural order (see the Supplemental Material [56]). Using different system sizes, we allow the formation of $n_l = 5$, 8, and 10 layers at high density and low temperature. In the following, we describe the properties of the eight-layer system and refer to other system sizes as needed.

At low temperatures, the 2D number density profile along the wall-to-wall separation coordinate z exhibits distinct peaks and no population between consecutive layers [Fig. 1(b)]. As the temperature increases, these peaks broaden and weaken, eventually merging into a uniform profile away from the attractive wall (Figs. S8 and S9 of the Supplemental Material [56]).

Snapshots [Fig. 1(c)] reveal a templating effect of the attractive wall on layer l_1, which in turn molds l_2, a pattern that propagates across layers (l_i for $i > 2$). The cascading "molding" effect is evident in adjacent layer pairs (Fig. S10 of the Supplemental Material [56]), where each layer fills the voids left by the one below it. The first peak of the

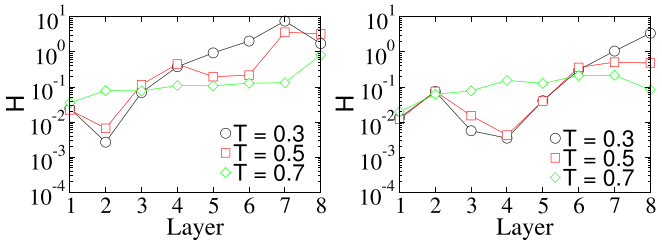

FIG. 2. Layer-by-layer hyperuniformity index H for slow annealing rate. Calculations are presented for systems at low ($\rho = 0.2$, left panel) and high ($\rho = 0.3$, right panel) density. H at $T = 0.3$ (black circles), $T = 0.5$ (red squares), and $T = 0.7$ (green rhombuses).

interlayer two-point correlation function $g_z(r)$ (Fig. S15 of the Supplemental Material [56]) appears at a distance greater than $R_R/a = 1.6$ for all couples of adjacent layers, which corresponds to the region where the interparticle potential is always attractive [see inset of Fig. 1(b)]. This confirms that the interlayer structural correlations are governed by energetically favorable particle arrangements.

A structured (crystallinelike) wall combined with a repulsive, structureless wall strongly modulates layer density, leading to a decreasing profile due to the attractive effect of the structured wall [Fig. 1(b), and Figs. S8 and S9 of the Supplemental Material [56]]. This effect persists across various attractive wall structures—including triangular and square lattices with different lattice constants ($d = a$ and $d = 1.5a$ for triangular, $d = a$ and $d = 1.25a$ for square)—and over a broad range of thermodynamic conditions. Such modulation is crucial for stabilizing competing structural arrangements within layers, as will be discussed in the forthcoming section. In particular, stripe (labyrinthine) phases form at specific layer densities, with estimates suggesting $\rho \simeq 0.53$ [2], matching our system (Fig. 3). These phases are observed across all attractive wall types (Figs. S11–S14 of the Supplemental Material [56]). In the following, we will focus on the triangular wall geometry with $d = a$, unless stated otherwise.

At low temperature ($T = 0.3$) and high density ($\rho = 0.3$), the confined fluid exhibits competing structural arrangements across layers [cf. Fig. 1(c), Figs. S10 and S11 of the Supplemental Material [56]]. The first layer forms a compact triangular lattice with pointlike and linear defects. Layer l_2 shows a mixture of triangular, kagome, honeycomb, and stripe phases, while layers l_3–l_7 are dominated by stripes increasingly interspersed with low-density triangular regions ($d \simeq R_R/a$). The eighth layer stabilizes into a low-density triangular lattice with void defects. Interestingly, l_1 and l_8 display isocrystalline structures—identical patterns with different lattice constants—arising from the CSW potential's soft shoulder, consistent with its known polymorphism and polyamorphism, as generally observed in isotropic soft-core potentials with two characteristic length scales [53]. At lower density ($\rho = 0.2$), a similar sequence occurs, except the compact triangular lattice in l_1 is suppressed and the low-density triangular lattice emerges already in l_3.

Given the distinctive features of each layer and their sharp separation at low T (see Figs. S8 and S9 of the Supplemental Material [56]), we analyze density fluctuations on a layer-by-layer basis. For each layer l_i, we compute the 2D structure factor $S(k)$, by projecting particle coordinates onto the xy plane, averaged over 5 (for slow annealing) to 10 (for fast annealing) independent quenches. We report the corresponding hyperuniformity index H for fast annealing and for each layer in Fig. 2.

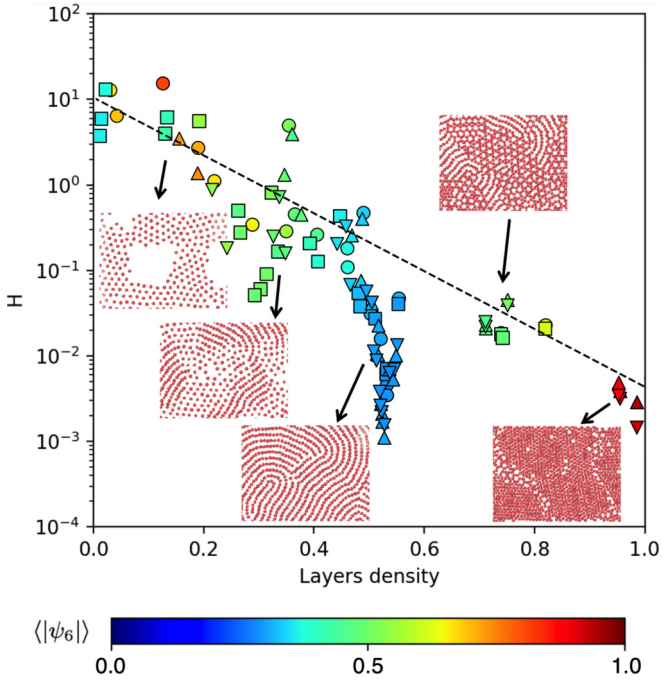

FIG. 3. Scaling of the hyperuniformity index H at different layer densities. Data, color coded by their $\langle|\psi_6|\rangle$ values, are for systems with eight and ten layers at $(\rho, T) = (0.2, 0.3)$ (circles), $(0.2, 0.5)$ (squares), $(0.3, 0.3)$ (upward triangles), $(0.3, 0.5)$ (downward triangles), and $\tau = t_0$, $10t_0$. While H is largely uncorrelated with $\langle|\psi_6|\rangle$ within the range $\in [0.4, 1]$, it exhibits an average exponential decrease over 5 orders of magnitude from a relatively large value of $H_0 = 11.37$ (the zero-density limit for H) toward $H \simeq 10^{-3}$, following $H_{\max} = H_0 \exp(-\rho/\rho_1)$ (black dashed line), with $\rho_1 = 0.13$. Notably, at $\rho \simeq 0.5$, H drops to a nearly hyperuniform value when $\langle|\psi_6|\rangle \simeq 0.3$, regardless of (ρ, T). The arrows indicate typical snapshots for each thermodynamic condition, showing compact triangular lattices with minimal defects ($\rho = 0.3$, $\tau = 10t_0$, $\langle|\psi_6|\rangle \simeq 1$) and stripe phases ($\langle|\psi_6|\rangle \simeq 0.3$) associated with emerging hyperuniformity.

Rapid quenches at low temperature yield structure factors decaying as $S(k) \sim k^\alpha$ ($\alpha > 0$) below a characteristic k^* in most layers [Fig. S1(b) of the Supplemental Material [56]], suggesting $H = 0$. The peak shown by $S(k)$ at the small value $k = k^*$ is associated with a characteristic length scale that is compatible, by visual inspection, with the typical distance between topological defects [see Fig. S1(c) of the Supplemental Material [56]]. The values of the exponent α for the different layers are in agreement with its estimation from the number variance $\sigma^2(R)$ [see Figs. S1(b) and S1(d) of the Supplemental Material [56]], which scales as $R^{D-\alpha}$ for $0 < \alpha < 1$ with $D = 2$ [51]. Under slower annealing [Fig. S1(a) of the Supplemental Material [56]], k^* is shifted toward smaller k indicating a larger characteristic length scale originating from a reduction of defects. As larger systems and improved statistics are

required for firm exponent estimates, to remain conservative, we report the hyperuniformity index $H = S(k \to 0)/S(k')$, with $S(k')$ taken at the highest peak and $S(k \to 0)$ extrapolated using a fourth-order even polynomial.

At low temperatures ($T = 0.3$ and $T = 0.5$), the profile of $H(l_i)$ is nonmonotonic, as shown in Fig. 2 for two densities, namely, $\rho = 0.2$ (left panel) and $\rho = 0.3$ (right panel). This nonmonotonic trend in H is the result of a general increase in disorder (and thus in H) as layer density decreases, and a sharp decrease in H associated with the emergence of stripelike configurations at low temperature and intermediate layer densities ($\rho_l \sim 0.5$), as also shown in Fig. 3. $H(l_i)$ varies significantly between $\simeq 10^{-3}$ and $\simeq 10$. Layers with $H \lesssim 10^{-2}$ typically exhibit either a defected triangular lattice or labyrinthine phases [e.g., l_3, l_4 in Fig. 1(c) for $\rho = 0.3$, and l_2 for $\rho = 0.2$, in Fig. S10 of the Supplemental Material [56]], akin to hyperuniform labyrinthlike structures in the Swift-Hohenberg model [57]. Layers with $10^{-2} < H < 1$ [e.g., l_2, l_5, l_6 in Fig. 1(c) for $\rho = 0.3$, and l_3, l_4, l_5 for $\rho = 0.2$, in Fig. S10 of the Supplemental Material [56]] display phase separation, while those with $H > 1$ (e.g., l_8 for $\rho = 0.3$, and l_6, l_7 for $\rho = 0.2$, in Fig. S10 of the Supplemental Material [56]) exhibit cavitation, where small-wavenumber density fluctuations resemble diverging $S(k \to 0)$ in antihyperuniform systems [51,58]. Defects, such as vacancies and dislocations, reduce hyperuniformity in proportion to their concentration [59]. In our system, just 2% random point defects in an otherwise perfect triangular lattice significantly lower hyperuniformity, and correlated defects, such as grain boundaries, suppress it further, with the H index rising with defect correlation and assuming values larger than those associated with liquid stripes arrangements (Figs. S6 and S7 of the Supplemental Material [56]).

At higher temperatures ($T = 0.7$), $H(l_i)$ saturates around $H \simeq 10^{-1}$ due to thermal noise, which induces interlayer diffusion and disrupts the fluid's layering, particularly for l_i with $1 < i < 8$ (Figs. S2–S4 of the Supplemental Material [56]). In the Supplemental Material [56], we further expand upon the mathematical properties of the number variance linked to the H index. The breadth of values acquired by the hyperuniformity index, which spans 4 orders of magnitude, upholds the large variety of properties that can be obtained within a single experiment.

For the eight-layer system, the averaged bond-orientational order $\langle|\psi_6|\rangle$ (see the Supplemental Material [56]) ranges from $\simeq 0.3$ in stripe phases to $\simeq 1$ in nearly defect-free triangular lattices (Fig. 3). Correspondingly, the H index decreases with density, reaching $\simeq 10^{-3}$. Strikingly, layers with local density $\simeq 0.5$ consistently form stripe patterns ($\langle|\psi_6|\rangle \simeq 0.3$) with H between 10^{-1} and 10^{-3}, marking the universal onset of hyperuniformity. Averaging over quenches suggests Class III hyperuniform stripes with $S(k) \propto k^{\alpha}, 0 < \alpha < 1$ [cf. Fig. S1(b) of the Supplemental Material [56]], though larger systems are needed for firm exponents.

We distinguish fluid- and solidlike layers via the 2D mean-square displacement (see the Supplemental Material [56]). At $\rho = 0.3$, all layers are solid at $T = 0.3$, while at $T = 0.5$ only l_1 and l_2 remain solid, the others becoming fluidlike (Fig. 4). Notably, both solid- and fluidlike layers can be nearly hyperuniform, consistent with rigidity-transition models in

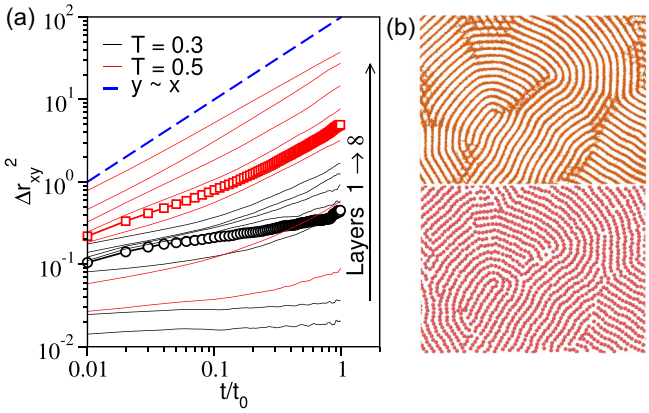

FIG. 4. Solid- and fluidlike layers. (a) 2D mean square displacement for $\tau = t_0$ at $\rho = 0.3$ and $T = 0.3$ (black) or $T = 0.5$ (red) for l_i with $i = 1, \ldots, 8$ from bottom to top. At $T = 0.3$ (black), all layers are solidlike, as indicated by $\langle(\Delta r_{xy})^2(t_0)\rangle < R_R^2 = 2.56$. At $T = 0.5$ (red), layers l_i with $i \geqslant 3$ exceed the 2.56 threshold, consistent with fluidlike, diffusive behavior (blue dashed line). Lines with symbols represent l_4, having a stripe structure at both temperatures. (b) At $T = 0.5$, the stripe phase in l_4 (bottom panel, showing a small portion of the xy snapshot at $t = 0$) evolves along fluidlike trajectories (wiggly lines in the top panel) over a time window t_0, while preserving the stripe pattern.

epithelial tissues [60]. This indicates that hyperuniformity is not tied to rigidity, but arises from cooperative motions preserving long-range correlations. For instance, l_4 at $T = 0.5$ remains nearly hyperuniform ($H \approx 3 \times 10^{-3}$) despite diffusive dynamics within stripe channels.

IV. CONCLUSIONS

In this work, we have performed large-scale molecular dynamics simulations at equilibrium conditions of the CSW fluid model, a general model that describes complex fluids such as globular proteins, soft colloids, and liquid metals. We demonstrate that confinement can modulate density fluctuations and tune the zero-wavenumber structure factor (isothermal compressibility) across a broad range of system conditions, stabilizing hyperuniform labyrinthine fluids and revealing a diverse array of emergent phases.

By systematically varying thermodynamic conditions, slit-pore width, and wall geometry, we induce layered structures with distinct long-range ordering spanning 4 orders of magnitude. These include (1) effectively hyperuniform layers appearing as defected crystals or labyrinthine stripe patterns, (2) nonhyperuniform layers characterized by coexisting crystalline patches of different symmetries and defects, indicative of a phase separation, and (3) antihyperuniform-like crystalline layers with extended and void defects (cavitation). These findings highlight the role of confinement in shaping structural complexity and regulating density fluctuations in self-assembled fluids. Our setup reveals labyrinthine stripe patterns as a universal arrangement that occurs across diverse working conditions and exhibits hyperuniform behavior. Such patterns have been widely observed in magnetic fluids and confined magnetic monolayers [61], amphiphilic monolayers, type I superconductors [62], block copolymer films [63], hard-sphere systems [64], and various biological

processes, including brain convolution development [65], fingerprint formation [66], and skin wrinkling [67], among others.

Finally, we anticipate that the stripe phase in the CSW model is linked to peaks in specific heat, as observed in 2D hard disks surrounded by a soft corona [68], despite its inclusion of an attractive term in the potential. While this term may alter phase stability, it is likely to do so only under conditions of extreme confinement [69]. However, the presence of multiple layers in our model complicates direct measurements, as confinement naturally selects the density of each layer. Additionally, we expect the heat capacity to exhibit multiple peaks at different densities, each corresponding to the formation of distinct phases in individual layers. Future studies will investigate how confinement affects phase transitions and thermodynamic anomalies, thereby further elucidating the role of geometric constraints in complex fluids.

ACKNOWLEDGMENTS

We thank Hugues Chaté, Andrea Gabrielli, and Salvatore Torquato for their valuable discussions. G.F. acknowledges funding by MICIU/AEI/10.13039/501100011033 and the European Commission "ERDF A way of making Europe" [grant numbers PID2021-124297NB-C31; PID2024-157478NB-C31]. E.C.O acknowledges support from Research Fund for International Scientists Grant by the National Natural Science Foundation of China (Grant No. 12350610238).

DATA AVAILABILITY

The data supporting this study's findings are available within the article.

[1] J. M. Drake and J. Klafter, Dynamics of confined molecular systems, Phys. Today **43**(5), 46 (1990).

[2] F. Leoni and G. Franzese, Structural behavior and dynamics of an anomalous fluid between attractive and repulsive walls: Templating, molding, and superdiffusion, J. Chem. Phys. **141**, 174501 (2014).

[3] F. Leoni, C. Calero, and G. Franzese, Nanoconfined fluids: Uniqueness of water compared to other liquids, ACS Nano **15**, 19864 (2021).

[4] J. Mittal, T. M. Truskett, J. R. Errington, and G. Hummer, Layering and position-dependent diffusive dynamics of confined fluids, Phys. Rev. Lett. **100**, 145901 (2008).

[5] M. C. Stewart and R. Evans, Phase behavior and structure of a fluid confined between competing (solvophobic and solvophilic) walls, Phys. Rev. E **86**, 031601 (2012).

[6] A. Zaragoza, M. A. González, L. Joly, I. López-Montero, M. A. Canales, A. L. Benavides, and C. Valeriani, Molecular dynamics study of nanoconfined TIP4P/2005 water: How confinement and temperature affect diffusion and viscosity, Phys. Chem. Chem. Phys. **21**, 13653 (2019).

[7] L. B. Krott and M. C. Barbosa, Anomalies in a waterlike model confined between plates, J. Chem. Phys. **138**, 084505 (2013).

[8] T. M. Truskett, P. G. Debenedetti, and S. Torquato, Thermodynamic implications of confinement for a waterlike fluid, J. Chem. Phys. **114**, 2401 (2001).

[9] A. Zaccone and K. Trachenko, Explaining the low-frequency shear elasticity of confined liquids, Proc. Natl. Acad. Sci. USA **117**, 19653 (2020).

[10] T.-D. Li and E. Riedo, Nonlinear viscoelastic dynamics of nanoconfined wetting liquids, Phys. Rev. Lett. **100**, 106102 (2008).

[11] I. Williams, E. C. Oğuz, T. Speck, P. Bartlett, H. Löwen, and C. P. Royall, Transmission of torque at the nanoscale, Nat. Phys. **12**, 98 (2016).

[12] C. Alba-Simionesco, B. Coasne, G. Dosseh1, G. Dudziak, K. E. Gubbins, R. Radhakrishnan, and M. Sliwinska-Bartkowiak, Effects of confinement on freezing and melting, J. Phys.: Condens. Matter **18**, R15 (2006).

[13] H. K. Christenson, Confinement effects on freezing and melting, J. Phys.: Condens. Matter **13**, R95 (2001).

[14] A. D. Virgiliis, R. L. C. Vink, J. Horbach, and K. Binder, Colloid-polymer mixtures between asymmetric walls: Evidence for an interface localization transition, Europhys. Lett. **77**, 60002 (2007).

[15] V. Kapil, C. Schran, A. Zen, J. Chen, C. J. Pickard, and A. Michaelides, The first-principles phase diagram of monolayer nanoconfined water, Nature (London) **609**, 512 (2022).

[16] P. Ravindra, X. R. Advincula, C. Schran, A. Michaelides, and V. Kapil, Quasi-one-dimensional hydrogen bonding in nanoconfined ice, Nat. Commun. **15**, 7301 (2024).

[17] S. Wan, X. Xi, H. Zhang, J. Ning, Z. Zheng, Z. Zhang, Y. Long, Y. Deng, P. Fan, D. Yang, T. Li, and A. Dong, Shape-mediated oriented assembly of concave nanoparticles under cylindrical confinement, ACS Nano **16**, 21315 (2022).

[18] B. de Nijs, S. Dussi, F. Smallenburg, J. D. Meeldijk, D. J. Groenendijk, L. Filion, A. Imhof, A. van Blaaderen, and M. Dijkstra, Entropy-driven formation of large icosahedral colloidal clusters by spherical confinement, Nat. Mater. **14**, 56 (2015).

[19] Y. Chen, Z. Yao, S. Tang, H. Tong, T. Yanagishima, H. Tanaka, and P. Tan, Morphology selection kinetics of crystallization in a sphere, Nat. Phys. **17**, 121 (2021).

[20] E. G. Teich, G. V. Anders, D. Klotsa, J. Dshemuchadse, and S. C. Glotzer, Clusters of polyhedra in spherical confinement, Proc. Natl. Acad. Sci. USA **113**, E669 (2016).

[21] F. Deißenbeck, H. Löwen, and E. C. Oğuz, Ground state of dipolar hard spheres confined in channels, Phys. Rev. E **97**, 052608 (2018).

[22] P. Ball and R. Evans, The density profile of a confined fluid, Mol. Phys. **63**, 159 (1988).

[23] J. F. Lutsko, Density functional theory of inhomogeneous liquids. II. A fundamental measure approach, J. Chem. Phys. **128**, 184711 (2008).

[24] R. Messina and H. Löwen, Reentrant transitions in colloidal or dusty plasma bilayers, Phys. Rev. Lett. **91**, 146101 (2003).

[25] L. B. Krott, T. Puccinelli, and J. R. Bordin, Core-softened colloid under extreme geometrical confinement, Soft Matter **20**, 4681 (2024).

[26] F. Martelli, H.-Y. Ko, C. C. Borallo, and G. Franzese, Structural properties of water confined by phospholipid membranes, Front. Phys. **13**, 136801 (2018).
[27] M. Chiricotto, F. Martelli, G. Giunta, and P. Carbone, Role of long-range electrostatic interactions and local topology of the hydrogen bond network in the wettability of fully and partially wetted single and multilayer graphene, J. Phys. Chem. C **125**, 6367 (2021).
[28] F. Martelli, J. Crain, and G. Franzese, Network topology in water nanoconfined between phospholipid membranes, ACS Nano **14**, 8616 (2020).
[29] Z. Wei, M. Chiricotto, J. D. Elliott, F. Martelli, and P. Carbone, Wettability of graphite under 2D confinement, Carbon **198**, 132 (2022).
[30] A. Gabrielli, M. Joyce, and F. S. Labini, Glass-like universe: Real-space correlation properties of standard cosmological models, Phys. Rev. D **65**, 083523 (2002).
[31] S. Torquato and F. H. Stillinger, Local density fluctuations, hyperuniformity, and order metrics, Phys. Rev. E **68**, 041113 (2003).
[32] S. Atkinson, G. Zhang, A. B. Hopkins, and S. Torquato, Critical slowing down and hyperuniformity on approach to jamming, Phys. Rev. E **94**, 012902 (2016).
[33] C. Laurent, P. M. Chaikin, J. P. Gollub, and D. J. Pine, Random organization in periodically driven systems, Nat. Phys. **4**, 420 (2008).
[34] C. E. Zachary, Y. Jiao, and S. Torquato, Hyperuniform long-range correlations are a signature of disordered jammed hard-particle packings, Phys. Rev. Lett. **106**, 178001 (2011).
[35] R. Xie, G. G. Long, S. J. Weigand, S. C. Moss, T. Carvalho, S. Roorda, M. Hejna, S. Torquato, and P. J. Steinhardt, Hyperuniformity in amorphous silicon based on the measurement of the infinite-wavelength limit of the structure factor, Proc. Natl. Acad. Sci. USA **110**, 13250 (2013).
[36] J. H. Weijs, R. Jeanneret, R. Dreyfus, and D. Bartolo, Emergent hyperuniformity in periodically driven emulsions, Phys. Rev. Lett. **115**, 108301 (2015).
[37] D. Hexner and D. Levine, Hyperuniformity of critical absorbing states, Phys. Rev. Lett. **114**, 110602 (2015).
[38] F. Martelli, S. Torquato, N. Giovambattista, and R. Car, Large-scale structure and hyperuniformity of amorphous ices, Phys. Rev. Lett. **119**, 136002 (2017).
[39] F. Carollo, J. P. Garrahan, I. Lesanovsky, and C. Pérez-Espigares, Fluctuating hydrodynamics, current fluctuations, and hyperuniformity in boundary-driven open quantum chains, Phys. Rev. E **96**, 052118 (2017).
[40] Q.-L. Lei, M. P. Ciamarra, and R. Ni, Nonequilibrium strongly hyperuniform fluids of circle active particles with large local density fluctuations, Sci. Adv. **5**, eaau7423 (2019).
[41] Y. Zheng, L. Liu, H. Nan, Z.-X. Shen, G. Zhang, D. Chen, L. He, W. Xu, M. Chen, Y. Jiao, and H. Zhuang, Disordered hyperuniformity in two-dimensional amorphous silica, Sci. Adv. **6**, eaba0826 (2020).
[42] T. Yanagishima, J. Russo, R. P. A. Dullens, and H. Tanaka, Towards glasses with permanent stability, Phys. Rev. Lett. **127**, 215501 (2021).
[43] F. Martelli, Steady-like topology of the dynamical hydrogen bond network in supercooled water, PNAS Nexus **1**, pgac090 (2022).
[44] M. Formanek, S. Torquato, R. Car, and F. Martelli, Molecular rotations, multiscale order, hyperuniformity, and signatures of metastability during the compression/decompression cycles of amorphous ices, J. Phys. Chem. B **127**, 3946 (2023).
[45] S. D. Cengio, R. Mari, and E. Bertin, Giant density fluctuations in locally hyperuniform states, Phys. Rev. E **112**, L042101 (2025).
[46] F. Martelli, B. G. Elmegreen, M. J. Zimoń, and K. M. Yeo, Hyperuniform and nearly hyperuniform neural networks, U.S. Patent Application US20240202508A1 (2024), https://patents.google.com/patent/US20240202508A1/en.
[47] Y. Wang, Z. Qian, H. Tong, and H. Tanaka, Hyperuniform disordered solids with crystal-like stability, Nat. Commun. **16**, 1398 (2025).
[48] N. Oppenheimer, D. B. Stein, M. Y. B. Zion, and M. J. Shelley, Hyperuniformity and phase enrichment in vortex and rotor assemblies, Nat. Commun. **13**, 804 (2022).
[49] Z. Ge, The hidden order of turing patterns in arid and semi-arid vegetation ecosystems, Proc. Natl. Acad. Sci. USA **120**, e2306514120 (2023).
[50] W. Hu, L. Cui, M. Delgado-Baquerizo, R. Solé, S. Kéfi, M. Berdugo, N. Xu, B. Wang, Q.-X. Liu, and C. Xu, Causes and consequences of disordered hyperuniformity in global drylands, Proc. Natl. Acad. Sci. USA **122**, e2504496122 (2025).
[51] S. Torquato, Hyperuniform states of matter, Phys. Rep. **745**, 1 (2018).
[52] P. Vilaseca and G. Franzese, Isotropic soft-core potentials with two characteristic length scales and anomalous behaviour, J. Non-Cryst. Solids **357**, 419 (2011).
[53] P. Vilaseca and G. Franzese, Softness dependence of the anomalies for the continuous shouldered well potential, J. Chem. Phys. **133**, 084507 (2010).
[54] F. Leoni and G. Franzese, Effects of confinement between attractive and repulsive walls on the thermodynamics of an anomalous fluid, Phys. Rev. E **94**, 062604 (2016).
[55] A. P. Thompson, H. M. Aktulga, R. Berger, D. S. Bolintineanu, W. M. Brown, P. S. Crozier, P. J. in 't Veld, A. Kohlmeyer, S. G. Moore, T. D. Nguyen, R. Shan, M. J. Stevens, J. Tranchida, C. Trott, and S. J. Plimpton, LAMMPS—A flexible simulation tool for particle-based materials modeling at the atomic, meso, and continuum scales, Comput. Phys. Commun. **271**, 108171 (2022).
[56] See Supplemental Material at http://link.aps.org/supplemental/10.1103/9xrg-4684 for additional details about the simulated model and supplementary analysis, which includes Ref. [70].
[57] Z. Ma and S. Torquato, Random scalar fields and hyperuniformity, J. Appl. Phys. **121**, 244904 (2017).
[58] E. C. Oğuz, J. E. S. Socolar, P. J. Steinhardt, and S. Torquato, Hyperuniformity and anti-hyperuniformity in one-dimensional substitution tilings, Acta Cryst. A **75**, 3 (2019).
[59] J. Kim and S. Torquato, Effect of imperfections on the hyperuniformity of many-body systems, Phys. Rev. B **97**, 054105 (2018).
[60] Y. Zheng, Y.-W. Li, and M. P. Ciamarra, Hyperuniformity and density fluctuations at a rigidity transition in a model of biological tissues, Soft Matter **16**, 5942 (2020).
[61] N. Osterman, D. Babic, I. Poberaj, J. Dobnikar, and P. Ziherl, Observation of condensed phases of quasiplanar core-softened colloids, Phys. Rev. Lett. **99**, 248301 (2007).

[62] A. J. Dickstein, S. Erramilli, R. E. Goldstein, D. P. Jackson, and S. A. Langer, Labyrinthine pattern formation in magnetic fluids, Science **261**, 1012 (1993).

[63] H. Feng, M. Dolejsi, N. Zhu, S. Yim, W. Loo, P. Ma, C. Zhou, G. S. W. Craig, W. Chen, L. Wan *et al.*, Optimized design of block copolymers with covarying properties for nanolithography, Nat. Mater. **21**, 1426 (2022).

[64] Y. Norizoe and T. Kawakatsu, Particle Monte Carlo simulation of string-like colloidal assembly in two and three dimensions, J. Chem. Phys. **137**, 024904 (2012).

[65] D. P. Richman, R. M. Stewart, J. Hutchinson, and V. S. Caviness, Mechanical model of brain convolutional development, Science **189**, 18 (1975).

[66] K. Efimenko, M. Rackaitis, E. Manias, A. Vaziri, L. Mahadevan, and J. Genzer, Nested self-similar wrinkling patterns in skins, Nat. Mater. **4**, 293 (2005).

[67] E. Cerda, K. Ravi-Chandar, and L. Mahadevan, Wrinkling of an elastic sheet under tension, Nature (London) **419**, 579 (2002).

[68] G. Malescio and G. Pellicane, Stripe phases from isotropic repulsive interactions, Nat. Mater. **2**, 97 (2003).

[69] F. Leoni and Y. Shokef, Attraction controls the inversion of order by disorder in buckled colloidal monolayers, Phys. Rev. Lett. **118**, 218002 (2017).

[70] S. Torquato, Structural characterization of many-particle systems on approach to hyperuniform states, Phys. Rev. E **103**, 052126 (2021).